Dynamics of a deformable self-propelled particle with internal rotational force

AUTHOR(S):

Tarama, M.; Ohta, T.

CITATION:

Tarama, M. ...[et al]. Dynamics of a deformable self-propelled particle with internal rotational force. Progress of Theoretical and Experimental Physics 2013, 2013(1): 13A01.

ISSUE DATE:

2013-01

URL:

http://hdl.handle.net/2433/173758

PTEP
Prog. Theor. Exp. Phys. **2013**, 013A01 (43 pages)
DOI: 10.1093/ptep/pts051

Dynamics of a deformable self-propelled particle with internal rotational force

Mitsusuke Tarama* and Takao Ohta

Department of Physics, Kyoto University, Kyoto, 606-8502, Japan
*E-mail: tarama@ton.scphys.kyoto-u.ac.jp

Received September 5, 2012; Revised October 19, 2012; Accepted October 19, 2012; Published January 1, 2013

We investigate the dynamics of a single deformable active particle that is accompanied by two types of internal force. One is related to the spontaneous propulsion of the center of mass and the other to the spontaneous spinning motion around the center of mass. The equations of motion are derived from the symmetry argument for the velocity of the center of mass, the traceless symmetric tensor variable characterizing the deformation, and the antisymmetric tensor variable for the spinning motion. Numerical simulations are carried out in both two and three dimensions to investigate the dynamics due to the coupling between migration, deformation, and spinning. Some of the bifurcations are studied by an analytical approach.

Subject Index A34, A54, A56

1. Introduction

Self-propulsion of micro-organisms such as living cells and bacteria is generally accompanied by shape deformation [1–4]. Deformable self-propelled motions have also been observed in non-biological systems of oil droplets floating on water, in which chemical reactions take place [5,6]. These phenomena provide us with a fascinating nonlinear and non-equilibrium problem. In fact, there are a substantial number of model systems for self-propelled motions. For example, elaborate theories for the shape deformation of migrating living matter have been developed for each specific biological object [7–9]. Simpler models for locomotion caused by shape deformation have also been introduced [10,11].

It is pointed out here that a spinning motion is also observed in many micro-organisms. A typical example is *Listeria*, which causes migration by actin polymerization and undergoes a helical motion (F.-L. Wen et al., unpublished work, and Refs. [12–15]). Flagellated bacteria such as *Escherichia coli* also exhibit a spinning motion by rotating helical filaments [16,17]. It is noted that, in these biological examples, the left-handed and right-handed symmetry is broken because the filament has a specific rotating direction. Quite recently, spontaneous formation of spiral waves in a *Dictyostelium* cell, was discovered, which is coupled with shape deformation, migration, and rotation of the cell (D. Taniguchi et al., unpublished work). It is also mentioned that there are experiments of spinning motion in non-biological systems. If a tiny solid soap is attached to the surface of an oily droplet, traveling motion and/or spinning motion are observed depending on the size of the attached soap (F. Takabatake et al., unpublished work, and Ref. [18]).

A few years ago, Ohta and Ohkuma introduced a model system for a deformable self-propelled particle [19]. This model does not rely on any specific living object but is derived by a general

symmetry argument between the velocity of the center of mass and deformation tensors. It is mentioned, however, that the set of time-evolution equations has been derived by a singular perturbation method from excitable reaction diffusion equations in both two and three dimensions [20,21]. Various dynamic motions of a self-propelled particle have been obtained from the coupled set of equations for migration and deformation [22,23].

As mentioned above, however, a spinning motion is another relevant degree of freedom in the motions of active matter. This is the basic motivation for the present study. That is, we investigate the dynamics of a deformable active particle that undergoes a spinning motion. We consider two types of activeness; one is spontaneous propulsion, which means that the center of mass of a particle undergoes translational movement due to the internal driving force. The other is the spontaneous spinning motion of the configuration of a particle around its center of mass. It is emphasized that the nonlinear coupling between migration, shape deformation, and spinning has not been studied so far. A spinning motion has been investigated theoretically but for a rigid self-propelled Brownian particle [24].

This paper is organized as follows. In Sect. 2, we introduce a set of time-evolution equations for a self-propelled soft particle with spinning degree of freedom. The dynamics in two dimensions are shown numerically in Sect. 3. The stability of spinless motion in the presence of a spinning disturbance is briefly discussed. Some of the results in two dimensions have been published [25]. Here we present only new results. The numerical results in three dimensions are described in Sect. 4. Some of the analysis in three dimensions is given in Sect. 5. The final section, Sect. 6, is devoted to a discussion. The technical details of the theory are given in the Appendix.

2. Time-evolution equations

Our analysis in this paper is based on the equations of motion derived from the symmetry argument for the velocity of the center of mass $\boldsymbol{v}$, a traceless symmetric tensor variable S_{ij} representing deformation, and an anti-symmetric tensor variable Ω_{ij} characterizing a spinning motion:

$$\frac{dv_i}{dt} = \gamma v_i - |v^2| v_i - a_1 S_{ij} v_j - a_2 \Omega_{ij} v_j \tag{1}$$

$$\frac{dS_{ij}}{dt} = -\kappa S_{ij} + b_1 (v_i v_j - \frac{1}{d}|v^2|\delta_{ij}) + b_2 (S_{ik}\Omega_{kj} - \Omega_{ik} S_{kj}) + b_3 \Omega_{ik} S_{kl} \Omega_{lj} \tag{2}$$

$$\frac{d\Omega_{ij}}{dt} = -\frac{\delta G}{\delta \Omega_{ij}} + c_1 (S_{ik}\Omega_{kj} + \Omega_{ik} S_{kj}) + c_2 S_{ik} \Omega_{kl} S_{lj} \tag{3}$$

where

$$G \equiv \frac{\zeta}{2} \mathrm{tr}\, \Omega_{ij}^2 + \frac{1}{4} \mathrm{tr}\, \Omega_{ij}^4 \tag{4}$$

and a_1, a_2, b_1, b_2, b_3, c_1, and c_2 are coupling constants. The parameters γ and ζ characterize the internal forces for spontaneous propulsion and for spontaneous spinning motion, respectively, and κ represents the relaxation rate of deformation. Here, we consider the case with positive κ, such that the shape of the particle becomes circular when there is no coupling between the shape deformation and the velocity or the spinning motion. d is the dimensionality of space.

The second rank traceless symmetric tensor S_{ij} represents an elliptical deformation in a two-dimensional space [19] and an ellipsoidal deformation in a three-dimensional space [23], which

is defined by

$$S_{ij} = \sum_m q^{(m)} n_i^{(m)} n_j^{(m)} \tag{5}$$

where $q^{(m)}$ and $\boldsymbol{n}^{(m)}$ are the eigenvalues and the corresponding eigenvectors of the tensor S_{ij}. Due to the traceless property of S_{ij}, the condition $\sum_m q^{(m)} = 0$ is required.

The antisymmetric tensor Ω_{ij}, which characterizes a spinning motion, is defined, in a two-dimensional space, by

$$\Omega_{ij} = \begin{bmatrix} 0 & \omega \\ -\omega & 0 \end{bmatrix}. \tag{6}$$

Then, the first term on the right-hand side in Eq. (3) is written as

$$-\frac{\delta G}{\delta \Omega_{ij}} = (\zeta - \omega^2)\Omega_{ij}. \tag{7}$$

In a three-dimensional space, Ω_{ij} is defined by

$$\Omega_{ij} = \epsilon_{ijk}\omega_k \tag{8}$$

where ϵ_{ijk} is the Levi–Civita symbol. The first term on the right-hand side of Eq. (3) is also given by Eq. (7) but with

$$\omega^2 = \omega_1^2 + \omega_2^2 + \omega_3^2. \tag{9}$$

The meaning of each coupling term in Eqs. (1)–(3) is as follows. The third term on the right-hand side of Eq. (1) and the second term on the right-hand side of Eq. (2) are the coupling of the velocity and the deformation to the leading order, where the deformation reduces the velocity (a_1 term) and the migration increases the deformation (b_1 term). These two terms also have the effect of bending the migration direction depending on the parameters. The last term on the right-hand side of Eq. (1) with $a_2 > 0$ corresponds to the force known as the Magnus effect, where a particle suffers a force in the direction perpendicular to that of the velocity and the angular momentum. As a result, the trajectory of a spinning particle tends to be curved. The third term on the right-hand side of Eq. (2) with $b_2 > 0$ represents the rotation of the configuration around $\boldsymbol{\omega}$. The fourth term on the right-hand side of Eq. (2) with $b_3 > 0$ has two effects; one is to enhance the deformation in the direction perpendicular to $\boldsymbol{\omega}$, and the other is to rotate the configuration around an axis perpendicular to $\boldsymbol{\omega}$. In two dimensions, the latter effect vanishes. The terms with the coefficient c_1 and c_2 on the right-hand side of Eq. (3) have the same effect on the vector $\boldsymbol{\omega}$ but, from the deformation, parallel and perpendicular to it, respectively. Therefore, the second term on the right-hand side of Eq. (3) with coefficient c_1 vanishes in two dimensions.

If the antisymmetric tensor variable Ω is not considered, the set of equations (1) and (2) has been derived from a symmetry argument and has been investigated both in two dimensions [19] and in three dimensions [23]. Moreover, these equations without the Ω variable have been derived from reaction–diffusion equations around drift bifurcation of a stationary localized domain [20,21]. It is noted that the dynamics of a deformable self-propelled particle under external forcing has also been investigated in a two-dimensional space [26].

In a previous paper [25], we have investigated the spinning dynamics in two dimensions obtained from Eqs. (1)–(3) by varying γ and b_3 with a fixed positive value of ζ. In this situation, the dynamics of a deformable self-propelled particle with a finite internal rotational force ζ has been considered. The coefficient γ governs the migration velocity and is a fundamental parameter. Our concern was

with the coupling between spinning motion and deformations. Therefore, we varied the coefficients b_3. In the present paper, we investigate the dynamics near the bifurcation threshold where the internal rotation Ω appears. In other words, we focus our attention on the bifurcation at which spinning motion occurs since experiments of the non-spinning state to the spinning state are expected (F. Takabatake et al., unpublished work, and Ref. [18]). Furthermore, we are mainly interested in the nonlinear coupling between spinning and deformations. Therefore, the nonlinearity of S and Ω is considered up to cubic order. To this end, all the coefficients, a_1, a_2, b_1, b_2, b_3, c_1, and c_2, are fixed, while the parameters γ and ζ are varied. The softness of the particle κ is also fixed throughout the present paper.

3. Dynamics in two dimensions

In this section, we investigate the emergence of the internal rotation in two dimensions. Due to the coupling of the internal translational force and the internal rotational force, the emergence of the internal rotation Ω is not so trivial around the region $\zeta \approx 0$ where the internal rotational force appears.

In a two-dimensional space, we use the representation $(v_1, v_2) = v(\cos\phi, \sin\phi)$, $S_{11} = -S_{22} = (s/2)\cos 2\theta$ and $S_{12} = S_{21} = (s/2)\sin 2\theta$. The time-evolution equations, Eqs. (1)–(3), can be written as

$$\frac{dv}{dt} = \gamma v - v^3 - \frac{a_1}{2} sv\cos 2\psi \tag{10}$$

$$\frac{d\phi}{dt} = -\frac{a_1}{2} s\sin 2\psi + a_2\omega \tag{11}$$

$$\frac{ds}{dt} = -\kappa s + b_1 v^2\cos 2\psi + b_3 s\omega^2 \tag{12}$$

$$\frac{d\theta}{dt} = -\frac{b_1}{2s} v^2\sin 2\psi + b_2\omega \tag{13}$$

$$\frac{d\omega}{dt} = (\zeta - cs^2)\omega - \omega^3 \tag{14}$$

where $\psi = \theta - \phi$ and $c = c_2/4$. From Eqs. (10)–(14), the dynamics is determined by v, s, ψ, ω. Therefore, we have only to solve Eqs. (10), (12), (14), and

$$\frac{d\psi}{dt} = -\left(\frac{b_1}{2s} v^2 - \frac{a_1}{2} s\right)\sin 2\psi - (a_2 - b_2)\omega. \tag{15}$$

The dynamics obtained from Eqs. (10)–(14) with a fixed strong internal spinning force $\zeta = 2$ has been investigated in our previous paper [25], where the internal propulsive force γ and the coefficient b_3 are varied. We have obtained a variety of dynamical states as well as motionless state: three types of orbital revolution, two quasi-periodic states, a period-doubling state, a chaotic state, and a spinning state. We have also carried out theoretical analysis of the bifurcation between some of these dynamical states by using the reduced coupled equations for two variables s and ψ obtained by eliminating other variables adiabatically.

Here, we are concerned with the emergence of the internal rotation Ω, i.e., we are interested in the dynamics around $\zeta \approx 0$. Therefore, in this section, we first consider the solutions of Eqs. (10)–(14) with $\omega = 0$ and the stability of those solutions. Then, we show the results of numerical simulations of Eqs. (10)–(14).

First, the stationary solutions of Eqs. (10)–(14) with $\omega = 0$ are simply the solutions of equations (1) and (2) without the Ω variable; these have been investigated previously [19]. When $\omega = 0$, stable solutions are given by $v = s = 0$ for $\gamma \le 0$, where a particle is motionless without any deformation.

On the other hand, for $\gamma > 0$, stable solutions of Eqs. (10), (12), and (15) with $\omega = 0$ are given by

$$v = \left(\frac{\gamma}{1 + B\cos^2 2\psi} \right)^{1/2} \tag{16}$$

$$s = \frac{b_1}{\kappa} v^2 \cos 2\psi \tag{17}$$

and $\tan 2\psi = 0$ for $0 < \gamma < \gamma_c$, where γ_c is given by [19]

$$\gamma_c = \frac{\kappa(1 + B)}{2B}. \tag{18}$$

Here, we have defined

$$B = \frac{a_1 b_1}{d\kappa}. \tag{19}$$

In contrast, for $\gamma \geq \gamma_c$, stable stationary solutions are given by Eqs. (16) and (17) and

$$\cos^2 2\psi = \frac{\kappa}{(2\gamma - \kappa)B}. \tag{20}$$

The former set of solutions represents the straight motion of a particle, while the latter corresponds to the circular motion. Its center of mass trajectory exhibits a closed circle.

For these solutions, we consider the stability condition of $\omega = 0$. From Eq. (14), it is evident that the condition $\omega = 0$ is valid as long as $\zeta - cs^2 \leq 0$. For the above motionless, straight, and circular states, this requirement is written as $\zeta \leq \zeta_0$, where

$$\zeta_0 = \begin{cases} 0 & \text{for } \gamma \leq 0 \\ c\dfrac{b_1^2 \gamma^2}{\kappa^2 (1 + B)^2} & \text{for } 0 < \gamma < \gamma_c \\ c\dfrac{b_1^2}{2\kappa B}\left(\gamma - \dfrac{\kappa}{2}\right) & \text{for } \gamma \geq \gamma_c. \end{cases} \tag{21}$$

The stability limit of the circular state has been calculated in our previous paper [25] and is consistent with Eq. (21). The bifurcation condition (21) should be compared with the results of numerical simulations.

Now, we show the results of the numerical simulations of Eqs. (10)–(14) in two dimensions. Since we are interested in the dynamics in the region $\zeta \approx 0$, we vary the internal spinning force ζ as well as the internal propulsion force γ. In numerical simulations, we fix the softness of the particle as $\kappa = 0.5$ and other coefficients as $a_1 = -1$, $a_2 = 0.75$, $b_1 = -0.5$, $b_2 = 1$, $b_3 = 1$, and $c = 1$.

In Fig. 1, we show the dynamical phase diagram. The regions indicated by the cross and the plus are defined as a motionless state and a frozen state, respectively. In both regions, the shape of the particle is circular without deformation, i.e. $s = 0$, and no migration occurs, $v = 0$. For the motionless state, the internal rotation does not exist $\omega = 0$, while there exists a finite internal rotation $\omega \neq 0$ for the frozen state. In the region indicated by the diamond, the shape of a particle is elliptically deformed but its center of mass is motionless, and there exists a finite internal rotation $\omega \neq 0$. We call this state a spinning state.

The filled square symbol in Fig. 1 represents a straight state with $\omega = 0$, where a particle propels straight with its shape elliptically deformed without internal rotation $\omega = 0$. In the region indicated by the open circle, an elliptically deformed particle undergoes an orbital revolution (circular motion) without internal rotation $\omega = 0$. This orbital revolution is due to the coupling of the spontaneous propulsion and the deformability of the particle. We call this state a circular state. In Figs. 2(a) and

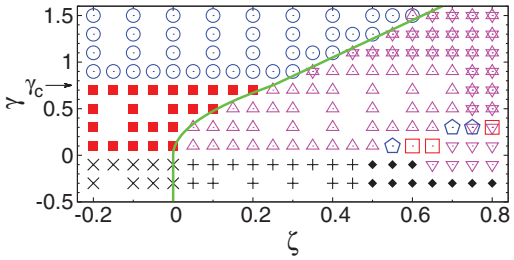

Fig. 1. Dynamical phase diagram obtained by solving Eqs. (1)–(3) numerically in two dimensions. The solid line is the stability limit of $\omega = 0$ given by Eq. (21). The bifurcation threshold $\gamma = \gamma_c$ $(= 0.75)$ between the straight state and the circular state is given by Eq. (18).

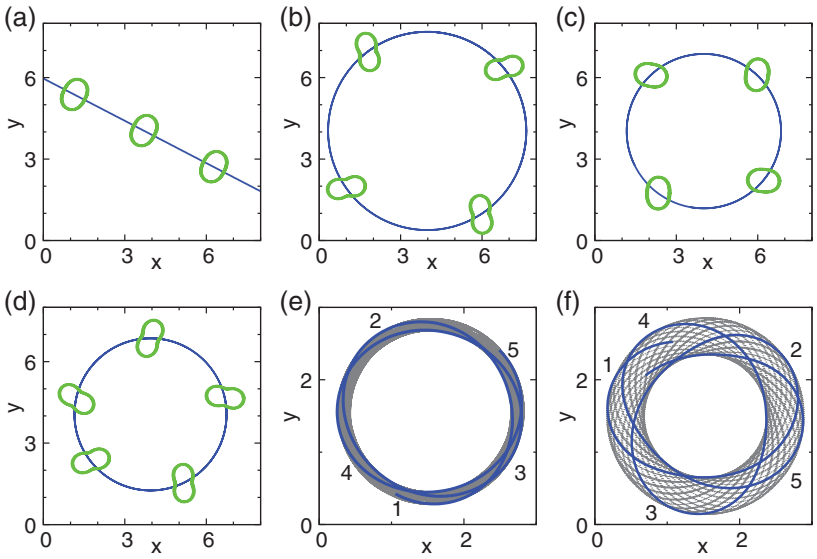

Fig. 2. Trajectories of (a) straight motion, (b) circular motion, (c) revolution I motion, (d) revolution II motion, (e) quasi-periodic I motion, and (f) quasi-periodic II motion, obtained by solving Eqs. (1)–(3) numerically in two dimensions. In Figs. (a)–(d), we also show some snapshots of the particle, which is reduced by the factor $1/4$ for the sake of clarity. A particle moves from left to right in Fig. (a) and in a counter-clockwise direction in Fig. (b)–(f). In Figs. (e) and (f), trajectories for shorter time intervals are indicated by the thick solid line with the chronological order 1–5.

(b), we show the trajectories in real space of the straight state for $\gamma = 0.5$ and $\zeta = 0$ and of the circular state for $\gamma = 1.5$ and $\zeta = 0.5$, respectively, where some snapshots of the particle are depicted. To draw the snapshots of the particle, the radius is set to be 2 throughout this section.

There also exist orbital revolutions with a finite internal rotation $\omega \neq 0$. The two kinds of triangles, up and down, in Fig. 1, represent the region where a particle undergoes an orbital revolution due to a finite internal rotation with its shape being elliptically deformed. The sign of ω can be both plus and minus depending on the initial condition, which corresponds to counter-clockwise and clockwise rotation. The difference of these two orbital revolutions with a finite value of ω is the direction of the deformation with respect to the velocity, given by the variable $\psi = \theta - \phi$. A particle in the region of the up triangle in Fig. 1 is deformed with $0 < \psi < \pi/2$ for $\omega > 0$, while the direction of the deformation of a particle in the region of the down triangle in Fig. 1 is given by $\pi/2 < \psi < \pi$ for $\omega > 0$. Here, note that ψ is π-periodic due to the symmetry of the deformation tensor S. The direction of the deformation for $\omega < 0$ is given by the relation $\pi - \psi$ with ψ for $\omega > 0$. We call

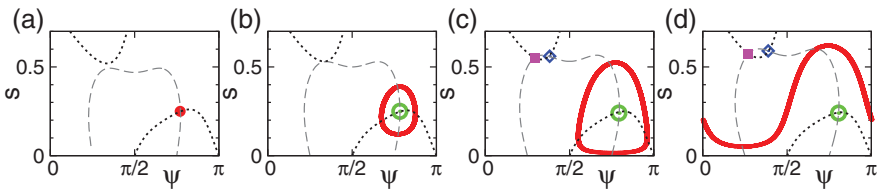

Fig. 3. Attractors in the s–ψ plane with $\omega > 0$, obtained by solving Eqs. (1)–(3) numerically in two dimensions. The filled circle and the filled square represent stable fixed points corresponding to the revolution I and II states respectively. The limit cycles in (b) and (c) are the attractors of the quasi-periodic I state, whereas the one in (d) represents the attractor corresponding to the quasi-periodic II state. The open circle and the open diamond represent the unstable fixed point and saddle point, respectively. We also show the s-nullcline and ψ-nullcline by the dashed line and the dotted line. The parameters are $\gamma = 1.3$ and (a) $\zeta = 0.65$, (b) $\zeta = 0.7$, (c) $\zeta = 0.75$, and (d) $\zeta = 0.8$.

these orbital revolution states in the up triangle region and in the down triangle region with finite ω the revolution I state and revolution II state, respectively. The trajectories in real space of the revolution I state for $\gamma = 0.5$ and $\zeta = 0.4$ and of the revolution II state for $\gamma = 1.3$ and $\zeta = 0.6$ are displayed in Figs. 2(c) and (d), respectively, with some snapshots of the particle. The value of ω is positive for both the revolution I and II states in Figs. 2(c) and (d), where the particle undergoes counter-clockwise revolution. The star in Fig. 1 is the superposition of the up and down triangles, where both the quasi-periodic I and II states coexist. There also exists a coexistence region for the revolution I state and the circular state at $\gamma = 1.5$ and $\zeta = 0.6$ in Fig. 1.

The pentagon symbol and the open square symbol in Fig. 1 represent quasi-periodic I and II states respectively. The trajectories in real space of these states are depicted in Fig. 2(e) for $\gamma = 0.3$ and $\zeta = 0.7$ and in Fig. 2(f) for $\gamma = 0.3$ and $\zeta = 0.8$, respectively. The value of ω is positive for both the revolution I and II states in Figs. 2(e) and (f), where the particle moves in a counter-clockwise direction. The difference of these two quasi-periodic states becomes clear in the s–ψ plane.

In Fig. 3, we show the attractors on the s–ψ plane corresponding to the revolution I and II states, the quasi-periodic I and II states with positive ω. These are obtained by solving numerically Eqs. (10)–(14) for $\gamma = 0.3$ and for different values of ζ, where s-nullcline and ψ-nullcline are superposed by the dashed and dotted lines. Figure 3(a) is obtained for $\zeta = 0.65$ with only one attractor, which is a stable fixed point corresponding to the revolution I state. In Fig. 3(b) for $\zeta = 0.7$, the fixed point (denoted by the open circle) becomes unstable, around which a stable limit cycle appears, corresponding to the quasi-periodic I state. On further increasing ζ, the attractor corresponding to the revolution II state, together with a saddle point, appears by a saddle node bifurcation; these are indicated by the filled square and the open diamond respectively in Fig. 3(c) for $\zeta = 0.75$. Finally, the quasi-periodic I state becomes unstable, and another stable limit cycle corresponding to the quasi-periodic II state appears, where the value of ψ varies from 0 to π monotonically as shown in Fig. 3(d) for $\zeta = 0.8$. See Ref. [25] for a more detailed investigation of these dynamical states and the bifurcations far from $\zeta \approx 0$ in two dimensions.

Finally, we show the stability limit of $\omega = 0$ for the motionless state, the straight state, and the circular states given by Eq. (21). It is superposed by the solid line in Fig. 1, which is in good agreement with the results of the numerical simulations. From the analytical form of the stability limit given by Eq. (21), it is clear that the straight state and the circular state without the internal rotation, $\omega = 0$, are stable even for small but positive values of ζ. This comes from the positiveness of c_2, which implies that the internal rotation makes the deformation of the particle unfavorable. We also note that there is no solution such that a particle moves straight with a finite value of ω.

Before closing this section, we mention the chaotic behavior of the particle. In our previous paper [25], we have found a period-doubling state and a chaotic state between the quasi-periodic I and II states for $\gamma = 1$ and $\zeta = 2$. In the present situation, however, we have found that there is no chaotic behavior or even a period-doubling state between the quasi-periodic I and II states in Fig. 1. One possible reason is that, in our previous paper [25], the parameter γ was chosen as $\gamma = 1$ to obtain the chaotic behavior. For this value of γ, the circular state appears in the absence of the internal rotation ω. In the present case, however, the parameter γ is choses as $\gamma = 0.1$ and 0.3 for the quasi-periodic I and II states. This is the straight state region in the absence of ω. The other possible reason is that the internal rotational force was strong ($\zeta = 2$) in Ref. [25], while here we are concerned with the region close to $\zeta \approx 0$. As we have discussed in Ref. [25], to realize a chaotic state, we need at least three variables s, ψ, and ω, namely softness of the particle, spontaneous orbital revolution due to the coupling of the velocity and the deformability, and spontaneous internal rotation. In the present case, we have chosen the parameter region such that the spontaneous orbital revolution is lacking and the spontaneous internal rotational force is small compared to our previous case [25]. These are expected to be the reasons for the lack of chaotic behavior between the revolution I and II states in Fig. 1.

4. Numerical simulations in three dimensions

In this section and in the next section, we investigate the dynamics of the time-evolution equations (1)–(3) in three dimensions.

If the antisymmetric tensor variable Ω is not considered, the set of equations (1) and (2) in three dimensions has four types of solutions [23]. One is a trivial solution given by $\boldsymbol{v} = \boldsymbol{0}$ and $S = 0$, where a particle with spherical shape is motionless. The motionless state is stable for $\gamma < 0$, but for $\gamma > 0$ a particle exhibits a spontaneous propulsion in a straight trajectory. The straight motion becomes unstable at $\gamma = \gamma_c$, where [23]

$$\gamma_c = \frac{\kappa(1+2B)}{3B} \tag{22}$$

with B defined by Eq. (19) with $d = 3$. Then, for $\gamma > \gamma_c$, the stable solution of Eqs. (1) and (2) is a circular state. This solution represents a particle that undergoes an orbital rotational motion on a closed circular trajectory on a two-dimensional plane embedded in a three-dimensional space. By increasing γ further, this circular state loses its stability at $\gamma = \gamma_h$, where [23]

$$\gamma_h = \frac{\kappa(1+B)}{B}. \tag{23}$$

Beyond the stability limit $\gamma > \gamma_h$, a particle undergoes helical motion.

Now, we consider the dynamics obtained when the internal rotational variable Ω is introduced to Eqs. (1) and (2). The internal rotation Ω is governed by Eq. (3). First, we show the numerical results. Since we are interested in the dynamics in the vicinity that the internal rotation Ω emerges as in two dimensions, we vary the strength of the translational and rotational internal forces, γ and ζ. The deformability is fixed as $\kappa = 0.5$ and the coupling coefficients as $a_1 = -1$, $a_2 = 0.75$, $b_1 = -0.5$, $b_2 = 1$, $b_3 = 1$, $c_1 = 1$, and $c_2 = 1$.

By numerically solving Eqs. (1)–(3), we have obtained several dynamical states, as summarized in Fig. 4, where the bifurcation thresholds γ_c and γ_h obtained without the spinning degree of freedom are also shown. In the region indicated by the cross and the plus symbols, a particle is motionless and its shape is spherical. In the cross region, the particle does not have internal rotation, i.e. $\Omega = 0$,

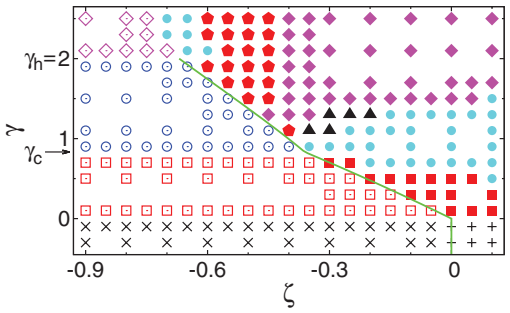

Fig. 4. Dynamical phase diagram obtained by solving Eqs. (1)–(3) numerically in three dimensions. The solid line is the bifurcation limit of $\omega = 0$ obtained analytically, as summarized in Table 1. The bifurcation threshold γ_c $(= 5/6)$ and γ_h $(= 2)$ between the straight and circular states for $\omega = 0$ and between the circular and helical states for $\omega = 0$ are given by Eqs. (22) and (23), respectively.

while a finite internal rotation exists in the plus region. We call the former state a motionless state and the latter a frozen state in a similar manner to the two-dimensional case.

In the region indicated by the open square, a straight state appears, where a particle whose shape is deformed from a sphere moves straight without internal rotation Ω. As the internal rotation does not exist, this straight state is nothing but the solution found in Ref. [23], where the antisymmetric tensor variable Ω is absent. On the other hand, the filled square symbol in Fig. 4 represents a spinning-straight state, which means that a deformed particle undergoes a straight motion with a finite internal rotation Ω. The trajectories in real space and the configurations of a particle of the straight state and of the spinning-straight state are shown in Figs. 5(a) and (b), which are obtained by solving Eqs. (1)–(3) for $\gamma = 0.3$ and $\zeta = -0.3$ and for $\gamma = 0.3$ and $\zeta = 0$ respectively. As shown in Fig. 5(a), the shape of the particle is symmetric with respect to the straight trajectory. In the spinning-straight state with a finite internal rotation Ω, the deformed shape of the particle is not symmetric around the velocity vector, and the direction of the internal rotation defined by $\boldsymbol{w}$ is parallel to the velocity as shown in Fig. 5(b). Therefore, a particle with a scalene-ellipsoidal shape spins around the straight trajectory.

The open circle in Fig. 4 denotes a circular state, where a particle undergoes an orbital revolution in a circular trajectory on a two-dimensional plane in three dimensions without the internal rotation Ω. The open diamond in Fig. 4 represents a helical state, where a particle undergoes spontaneous propulsion in a helical trajectory without internal rotation Ω. As the internal rotation does not exist, these two dynamical states are the same as those found in Ref. [23], without the antisymmetric tensor variable Ω. The trajectories in real space and the configurations of the circular state and the helical state are shown in Figs. 6(a) and (b) respectively.

There are two other types of helical motion; one is a helical motion with a finite internal rotation Ω, which exists in the region of the closed diamond in Fig. 4. In this state, a particle undergoes a spontaneous propulsion in a helical trajectory with a finite constant internal rotation. Therefore, we call this motion spinning-helical motion. The trajectory and the shape of the particle are shown in Fig. 6(c). The other helical motion is called an oscillating-helical state, obtained for the parameters indicated by the filled circle in Fig. 4. In this state, the value of the internal rotation, as well as the value of the velocity and the magnitude of the deformation, undergoes oscillation in time with the same period, which will be discussed at the end of this section. The trajectory and the shape of the particle are depicted in Figs. 6(d) and (e), which are obtained numerically for (d) $\gamma = 1.3$ and $\zeta = -0.1$ and for (e) $\gamma = 2.3$ and $\zeta = -0.65$, respectively. Since the parameter region of this state

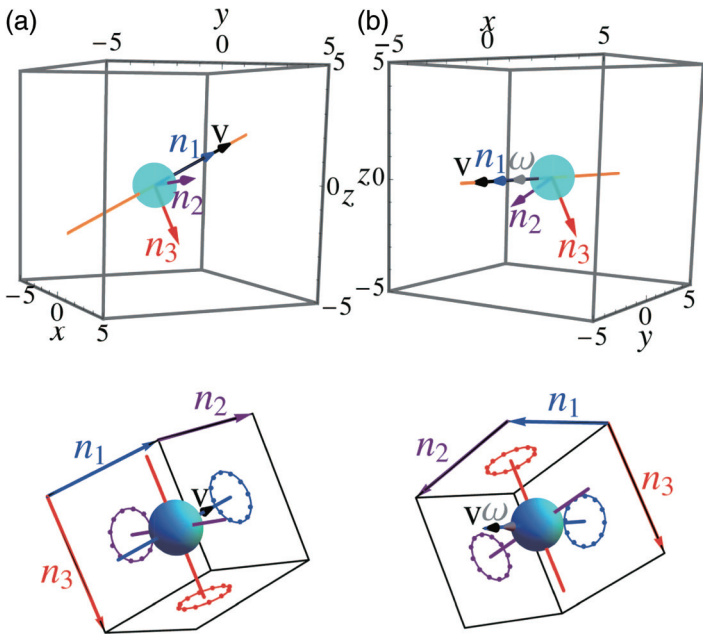

Fig. 5. Trajectory in real space (TOP) and close-up snapshot of the configuration of a particle (DOWN) of (a) the straight state and (b) the spinning-straight state obtained by solving Eqs. (1)–(3) numerically. Projected figures of the configuration onto the plane perpendicular to the eigenvectors $\boldsymbol{n}_m$ of the deformation tensor S are also displayed by the solid line, together with the dotted lines, representing a circular profile without deformation. The parameters are set as $\gamma = 0.3$ and (a) $\zeta = -0.3$ and (b) $\zeta = 0$. In this figure and in Fig. 6 below, we use the notation $\boldsymbol{n}_m = \boldsymbol{n}^{(m)}$, the latter part of which appears in Eq. (5). These unit vectors are defined such that the corresponding eigenvalues are in the order $q^{(1)} < q^{(2)} < q^{(3)}$.

in Fig. 4 is separated into two, we show the trajectories and configurations for the parameters of each region.

The region indicated by the filled pentagon in Fig. 4 represents a superhelical state, where a particle moves in a superhelical trajectory with a finite internal rotation Ω. The trajectory and the shape are displayed in Fig. 6(f), obtained numerically from Eqs. (1)–(3) for $\gamma = 2.3$ and $\zeta = -0.55$. In Fig. 7(a), we also show the trajectory in real space for a longer time interval, where the superposed box indicates the region plotted in Fig. 6(f). The value of the velocity and the internal rotation of the particle, as well as its shape, oscillate in time with the same period, as discussed later.

Finally, there also exists a chaotic behavior for parameters displayed by the filled triangles in Fig. 4. The trajectory in real space is shown in Fig. 7(b) for $\gamma = 1.3$ and $\zeta = -0.3$. In order to elucidate the chaotic behavior, we tried to calculate the maximum Lyapunov exponent numerically. However, we could not estimate it accurately due to the large variance. Therefore, we put a small perturbation onto each variable in phase space and calculated the time evolution of the deviation of the trajectory in real space from that of the non-perturbed case. In Fig. 8, we show the result for the chaotic state for $\gamma = 1.3$ and $\zeta = -0.3$. For comparison, we also show the result for the spinning-helical state for $\gamma = 1.5$ and $\zeta = -0.3$. From this result, it seems that the deviation of the trajectory of the chaotic state increases as $\sim t^{0.5}$, while that of the spinning-helical state does not increase. Here, note that the oscillating behavior of the displacement of the spinning-helical state was obtained for the period different from nT_h with n some integer, where T_h is the period for a particle to move one pitch of the helical trajectory. That is, when the perturbation is added to the phase variables of the spinning-helical state, then after relaxation, the particle again moves in a helical trajectory, whose axis is almost

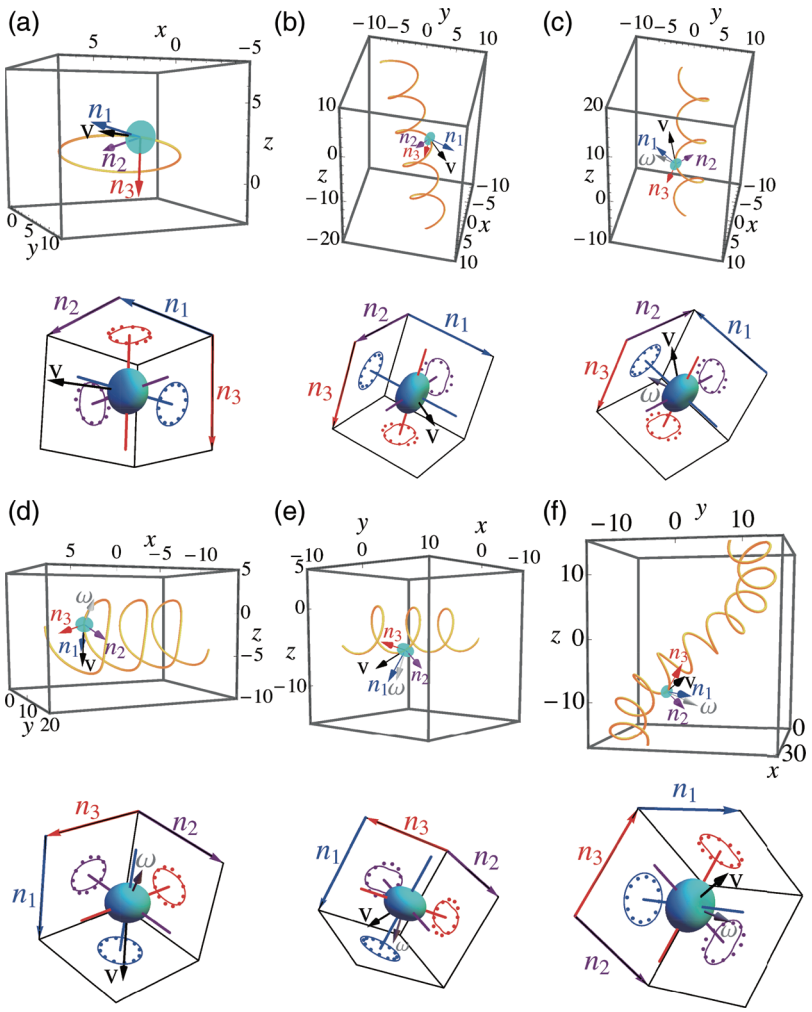

Fig. 6. Trajectory in real space and snapshot of the configuration of the particle of (a) the circular state for $\gamma = 1.3$ and $\zeta = -0.6$, (b) the helical state for $\gamma = 2.3$ and $\zeta = -0.8$, (c) the spinning-helical state for $\gamma = 2.3$ and $\zeta = -0.4$, (d) and (e) the oscillating-helical state for $\gamma = 1.3$ and $\zeta = -0.1$ and for $\gamma = 2.3$ and $\zeta = -0.65$, and (f) the superhelical state for $\gamma = 2.3$ and $\zeta = -0.55$.

parallel to that of the non-perturbed case, but with a slightly different position in space. Therefore, if we calculate the distance between two particles moving on those trajectories with a time interval different from nT_h, it is natural that the distance oscillates. On the other hand, for the chaotic state, the displacement of the trajectories in real space increases, which is typical behavior for chaotic motion against a small perturbation. In an ordinary chaotic state, the deviation increases exponentially [27]. We do not have any explanation of this power law behavior with exponent 0.5 but will return to this problem in Sect. 6.

Before closing this section, we briefly mention the periodic behavior of the oscillating-helical state and the superhelical state. Unlike the other dynamical states, the magnitude of the velocity, the deformation, and the internal rotation of these two states oscillate in time with a period T_p. From the result of the numerical simulation, we have obtained a relation between T_p and T_h, where T_h is the period for a particle to move one pitch of the helical trajectory. For the oscillating-helical state, the relation is given by $2T_p = T_h$, whereas it becomes $T_p = T_h$ for the superhelical state. Here, note that, for the superhelical state, T_h should be calculated for a particle to move one pitch of a 'small' helical

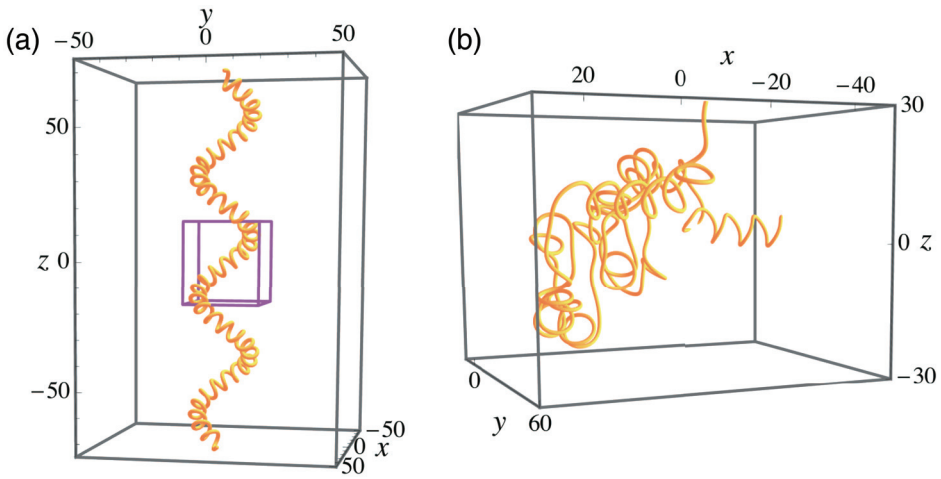

Fig. 7. Trajectory in real space of (a) the superhelical state and (b) the chaotic state for long time intervals, obtained by solving Eqs. (1)–(3) numerically. In (a), the superposed box indicates the plot region of the trajectory in Fig. 6(f). Parameters are set as (a) $\gamma = 2.3$ and $\zeta = -0.55$ and (b) $\gamma = 1.3$ and $\zeta = -0.3$.

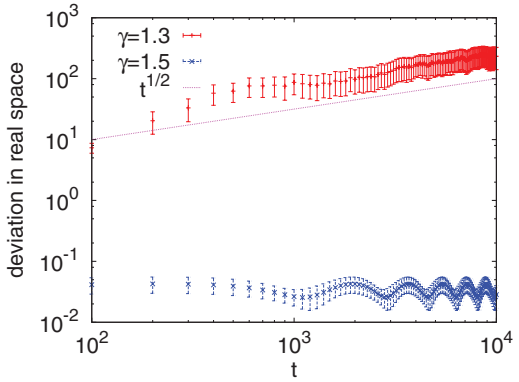

Fig. 8. Time-evolution of the deviation of the trajectory in real space against a small perturbation of the chaotic state for $\gamma = 1.3$ and $\zeta = -0.3$. For comparison, we also show the time evolution of the displacement of the spinning-helical state for $\gamma = 1.5$ and $\zeta = -0.3$.

structure, i.e. the helical structure shown in Fig. 6(f). We have no theoretical derivation for these relations at present.

5. Analysis of the emergence of internal rotation in three dimensions

In this section, we develop a theoretical analysis of the emergence of the internal rotation Ω in three dimensions. Generally, we can write the velocity vector in terms of its magnitude and direction as $v_i = vu_i$. Three components ω_i of the anti-symmetric tensor Ω can also be written as $\omega_i = \omega w_i$, where ω is defined by Eq. (9). The time-evolution equations, Eqs. (1)–(3), are written as

$$\frac{dv}{dt} = \gamma v - v^3 - a_1 v \sum_m q^{(m)} P_m^2 \tag{24}$$

$$\frac{du_i}{dt} = -a_1 \sum_m q^{(m)} (P_m n_i^{(m)} - P_m^2 u_i) - a_2 \epsilon_{ijk} u_j \omega_k \tag{25}$$

$$\frac{dq^{(n)}}{dt} = -\kappa q^{(n)} + b_1 v^2 \left(P_n^2 - \frac{1}{3} \right) - b_3 \sum_{m \neq n} q^{(m)} (\epsilon_{ijk} n_i^{(m)} n_j^{(n)} \omega_k)^2 \tag{26}$$

$$\frac{dn_i^{(n)}}{dt} = \sum_{m \neq n} \frac{b_1 v^2}{q^{(n)} - q^{(m)}} P_n P_m n_i^{(m)} - b_2 \epsilon_{ijk} n_j^{(n)} \omega_k - b_3 \omega^2 \sum_{m \neq n} \frac{q^{(n)} + q^{(m)}}{q^{(n)} - q^{(m)}} Q_n Q_m n_i^{(m)} \tag{27}$$

$$\frac{d\omega}{dt} = (\zeta - \omega^2)\omega - c_1 \sum_m q^{(m)} \omega Q_m^2 + c_2 \sum_m q^{(m')} q^{(m'')} \omega Q_m^2 \tag{28}$$

$$\frac{dw_i}{dt} = \sum_m (-c_1 q^{(m)} + c_2 q^{(m')} q^{(m'')})(Q_m n_i^{(m)} - Q_m^2 w_i) \tag{29}$$

where it is required that the indices m' and m'' on the right-hand side of Eqs. (28) and (29) should be chosen to satisfy $\epsilon^{mm'm''} = 1$. Here, we have defined

$$P_n = n_i^{(n)} u_i \tag{30}$$

$$Q_n = n_i^{(n)} w_i. \tag{31}$$

As we have mentioned, if the internal rotation $\boldsymbol{\omega} = \omega \boldsymbol{w}$ is not considered, Hiraiwa et al. have found [23] that the set of the time-evolution equations (24)–(27) have four types of solutions: the motionless state, the straight state, the circular state, and the helical state. The analytical form of the motionless state, which is stable as long as $\gamma < 0$, is given by $v = 0$ and $q^{(n)} = 0$ for $n = 1$, 2, and 3 [23]. If $\gamma > 0$, one of the stable solutions is the straight motion, which is described as [23]

$$v^2 = \frac{\gamma}{1 + 2B} \tag{32}$$

$$q^{(1)} = \frac{2b_1 v^2}{3\kappa}, \; q^{(2)} = q^{(3)} = -\frac{b_1 v^2}{3\kappa} \tag{33}$$

$$P_1 = 1, \; P_2 = P_3 = 0. \tag{34}$$

This stationary solution is stable as long as $0 < \gamma < \gamma_c$, where γ_c is given by Eq. (22). For larger values of γ, the stable solution is given by [23]

$$v^2 = \frac{2\gamma}{2 + B + 3B\mathcal{P}^2} = \frac{2\gamma - \kappa}{2 + B} \tag{35}$$

$$q^{(1,2)} = \frac{b_1 v^2}{2\kappa} \left(\frac{1}{3} \pm \mathcal{P} \right), \; q^{(3)} = -\frac{b_1 v^2}{3\kappa} \tag{36}$$

$$P_{1,2}{}^2 = \frac{1}{2}(1 \pm \mathcal{P}), \; P_3 = 0 \tag{37}$$

where

$$\mathcal{P}^2 = \frac{\kappa(2 + B)}{3B(2\gamma - \kappa)}. \tag{38}$$

This solution corresponds to the circular state. The stability condition of this circular state is given by $\gamma_c < \gamma < \gamma_h$, where γ_h is defined by Eq. (23). Finally, for $\gamma > \gamma_h$, the stable solution is a helical state, where the trajectory in real space is a helix. The analytical form of this solution has not been obtained [23].

These stationary solutions, together with $\boldsymbol{\omega} = \mathbf{0}$, consist of stationary solutions of Eqs. (1)–(3), where the Ω variable is taken into consideration. Hereafter, we exploit the stability condition of $\omega = 0$ for these stationary solutions, which is given from Eq. (28) by

$$\zeta - c_1 \sum_m q^{(m)} Q_m^2 + c_2 \sum_m q^{(m')} q^{(m'')} Q_m^2 < 0. \tag{39}$$

To obtain the concrete form of Eq. (39), we need to calculate the value of the scalar product $Q_m = n_i^{(m)} w_i$ for the stationary solutions. Although $\omega = 0$ for the motionless, straight, circular, and helical states, we may define $w_i = \omega_i/\omega$ around the bifurcation boundary. From Eqs. (27) and (29), we obtain

$$\begin{aligned} \frac{dQ_n}{dt} = & \sum_{m\neq n} \frac{b_1 v^2}{q^{(n)} - q^{(m)}} P_n P_m Q_m - \sum_{m\neq n} b_3 \omega^2 \frac{q^{(n)} + q^{(m)}}{q^{(n)} - q^{(m)}} Q_m^2 Q_n \\ & - (c_1 q^{(n)} - c_2 q^{(n')} q^{(n'')}) Q_n + \sum_m (c_1 q^{(m)} - c_2 q^{(m')} q^{(m'')}) Q_m^2 Q_n \end{aligned} \tag{40}$$

where the indices n' and n'', and m' and m'' in the third and fourth terms on the right-hand side should be chosen to satisfy $\epsilon^{nn'n''} = 1$ and $\epsilon^{mm'm''} = 1$, respectively.

For the motionless state, where $v = 0$ and $q^{(n)} = 0$ for $n = 1, 2, 3$, the only stationary solution of Eq. (40) is $Q_n = 0$. Therefore, the stability condition of $\omega = 0$ is given from Eq. (39) by $\zeta < 0$. For the straight state represented by Eqs. (32)–(34), Eq. (40) has two sets of stable solutions. Together with these solutions, the stability condition of $\omega = 0$ for the straight state is given from Eq. (39) by

$$\zeta < \zeta_{st}^- = 2c_1 \frac{b_1\gamma}{3\kappa(1+2B)} - c_2 \left(\frac{b_1\gamma}{3\kappa(1+2B)} \right)^2 \tag{41}$$

as long as $L_1 > 0$, where

$$L_1 = -\frac{b_1 v^2}{\kappa} \left(c_1 - c_2 \frac{b_1\gamma}{3\kappa(1+2B)} \right). \tag{42}$$

Otherwise, the stability condition becomes

$$\zeta < \zeta_{st}^+ = -c_1 \frac{b_1\gamma}{3\kappa(1+2B)} + 2c_2 \left(\frac{b_1\gamma}{3\kappa(1+2B)} \right)^2. \tag{43}$$

See the Appendix for the detailed derivation of the stability condition of $\omega = 0$ for the straight state.

Next, we consider the stability condition of $\omega = 0$ for the circular state. For the circular motion on a plane described by Eqs. (35)–(37), there are three types of stable solutions of Eq. (40). From the analytical form of these solutions, the stability condition of $\omega = 0$ is described as follows. First, when $E_\eta > 0$ and

$$2\mathcal{C}_+ - E_\eta^{1/2} < 0 \tag{44}$$

are satisfied, the stability condition of $\omega = 0$ is obtained as

$$\zeta < \zeta_c^- = \frac{b_1 v^2}{6\kappa} \left(c_1 + c_2 \frac{b_1 v^2}{3\kappa} \right) - \frac{1}{2} E_\eta^{1/2}. \tag{45}$$

Here, we have defined

$$E_\eta = 4\mathcal{C}_-^2 - \left(\frac{\kappa}{\mathcal{P}} \right)^2 (1 - \mathcal{P}^2) \tag{46}$$

Table 1. Bifurcation threshold ζ from $\omega = 0$ to finite ω for the motionless state (M), the straight state (St), and the circular state (C) in three dimensions. $\omega = 0$ is stable for ζ less than the threshold. For the helical state without the internal rotation Ω (H), the analytical form of the stability condition of $\omega = 0$ has not been obtained.

H		x
C	ζ_c^+	if $\mathcal{C}_+ > 0$ and $\mathcal{C}_+^2 - E_\eta/4 > 0$
	ζ_c^0	if $\mathcal{C}_+ < 0$ and $E_\eta < 0$
	ζ_c^-	if $\mathcal{C}_+ - E_\eta^{1/2}/2 < 0$ and $E_\eta > 0$
St	ζ_{st}^+	if $L_1 < 0$
	ζ_{st}^-	if $L_1 > 0$
M		0

and

$$\mathcal{C}_+ = \frac{b_1 v^2}{2\kappa}\left\{c_1 + c_2\frac{b_1 v^2}{2\kappa}\left(\frac{1}{3} - \mathcal{P}^2\right)\right\} \tag{47}$$

$$\mathcal{C}_- = \frac{b_1 v^2}{2\kappa}\left(c_1 - c_2\frac{b_1 v^2}{3\kappa}\right)\mathcal{P}. \tag{48}$$

If E_η is negative, the stability condition of $\omega = 0$ is given by

$$\zeta < \zeta_c^0 = \frac{b_1 v^2}{6\kappa}\left(c_1 + c_2\frac{b_1 v^2}{3\kappa}\right). \tag{49}$$

This stability condition is valid as long as $\mathcal{C}_+ < 0$. Finally, for the parameters satisfying $\mathcal{C}_+ > 0$ and

$$\mathcal{C}_+^2 - \frac{1}{4}E_\eta > 0 \tag{50}$$

the stability condition of $\omega = 0$ is calculated as

$$\zeta < \zeta_c^+ = \frac{b_1 v^2}{3\kappa}\left\{-c_1 + c_2\frac{b_1\,(4\gamma_h - \gamma - 3\gamma_c)}{6\kappa\,(2 + B)}\right\}. \tag{51}$$

Again, the detailed derivation of Eqs. (45), (49), and (51) is described in the Appendix. Since an analytical solution for the helical state with $\omega = 0$ has not been obtained, we do not investigate the stability of $\omega = 0$ for this state here.

Finally, the emergence of the internal rotation Ω in a three-dimensional space obtained above is summarized in Table 1. In Fig. 4, we show the bifurcation lines given in Table 1 by a solid line; they are in good agreement with the numerical results. Here, note that, for the parameters chosen to obtain the numerical results in Sect. 4, the bifurcation line is given by ζ_{st}^- for the straight state, and ζ_c^- for the circular state.

6. Discussion

In this paper, we have investigated the dynamics of a deformable self-propelled particle with spontaneous spinning motion in both two and three dimensions. We have considered two different types of activeness; one is spontaneous propulsion, i.e., the center of mass of a particle undergoes translational movement due to its internal driving force. The other is the spontaneous spinning motion of

the configuration of a particle around its center of mass. In our previous paper [25], we have investigated the dynamics of a deformable self-propelled particle with a finite internal rotational force in a two-dimensional space. In contrast, in this paper, we are interested in and concerned with the dynamics around the emergence of the internal rotation.

In a two-dimensional space, we have carried out stability analysis of the internal rotation for the motionless, straight, and circular states, where the internal rotation does not exist, i.e. $\omega = 0$. We have also solved the time-evolution equations (1)–(3) numerically, and obtained a rich variety of dynamical states as summarized in a dynamical phase diagram for $\kappa = 0.5$ displayed in Fig. 1. Apart from the motionless, straight, and circular states, we have found two types of orbital revolution states, two types of quasi-periodic states, a frozen state, and a spinning state when a finite internal rotation exists. The trajectories in real space of the straight state, three types of revolution states including the circular state, and two quasi-periodic states are depicted in Fig. 2.

The dynamics in three dimensions has also been investigated. From the numerical simulations of Eqs. (1)–(3), we have obtained a dynamical phase diagram for $\kappa = 0.5$, including various fascinating dynamical states, as shown in Fig. 4. There exist a circular state, two types of straight states, three types of helical states, and a superhelical state, as well as a motionless state and a frozen state. For the former seven orbital motions, the trajectories in real space and a close-up snapshot of the configuration of the particle are displayed in Fig. 5, Fig. 6, and Fig. 7(a). Even a chaotic behavior has been found, whose trajectory in real space is shown in Fig. 7(b). In order to elucidate the chaotic motion, we have used perturbation for the phase variables and have calculated the expansion behavior of the deviation of the trajectories in real space with respect to that of the non-perturbed case. As a result, we have found that the displacement is not exponential but obeys a power law $\sim t^{0.5}$. The slow divergence of the separation of two nearby trajectories has been investigated in terms of weak chaos, where the maximum Lyapunov exponent becomes zero, though it is reported as subexponential [28,29]. From the viewpoint of transport and mixing, the growth of the displacement variance of a passive particle in turbulence has been found to obey a power law, where the intermittency plays an important role [30]. For the chaotic motion found in this paper, although we could not estimate the maximum Lyapunov exponent due to the large variance, the trajectory appears to be intermittent as shown in Fig. 7(b). At present, however, we have no explanation for this power law behavior, which will be investigated separately in the near future.

Acknowledgments

This work was supported by the JSPS Core-to-Core Program "International research network for non-equilibrium dynamics of soft matter" and by a Grant-in-Aid for Scientific Research C (No. 23540449) from JSPS. We are also grateful for a Grant-in-Aid for the Global COE Program "The Next Generation of Physics, Spun from Universality and Emergence" from the Ministry of Education, Culture, Sports, Science and Technology (MEXT) of Japan. M.T. is supported by the Japan Society for the Promotion of Science Research Fellowship for Young Scientists.

Appendix

In this appendix, we derive the stability condition of $\omega = 0$ given by Eq. (39) for the straight state and for the circular state in three dimensions. To this end, we need to obtain the solutions of Eq. (40) for these states respectively.

For the straight state represented by Eqs. (32)–(34), Eq. (40) becomes

$$\frac{dQ_1}{dt} = L_1(1 - Q_1^2)Q_1 \tag{A.1}$$

$$\frac{dQ_2}{dt} = -L_1 Q_1^2 Q_2 \tag{A.2}$$

$$\frac{dQ_3}{dt} = -L_1 Q_1^2 Q_3 \tag{A.3}$$

where L_1 is given by Eq. (42). There are two stationary solutions; one is given by $(Q_1, Q_2, Q_3) = (1, 0, 0)$ and the other by $Q_1 = 0$ with Q_2 and Q_3 satisfying $Q_2^2 + Q_3^2 = 1$. The former solutions are stable as long as the coefficient L_1 is positive, where the latter is unstable. If L_1 is negative, the former solutions become unstable, while the stability of the latter solutions is neutral. That is, $Q_1 = 0$ is stable whereas the linear stability of Q_2 and Q_3 are neutral. However, this is not strange because, from Eq. (33), the particle is uniaxial and its shape is symmetric around $\boldsymbol{n}^{(1)}$. Therefore, the other eigenvectors $\boldsymbol{n}^{(2)}$ and $\boldsymbol{n}^{(3)}$ cannot be determined uniquely. The stable stationary solution $Q_1 = n_i^{(1)} w_i = 0$ means that the vector $\boldsymbol{w}$ is perpendicular to $\boldsymbol{n}^{(1)}$, and, hence, it lays on the plane spanned by the vectors $\boldsymbol{n}^{(2)}$ and $\boldsymbol{n}^{(3)}$. Since the spanning vectors $\boldsymbol{n}^{(2)}$ and $\boldsymbol{n}^{(3)}$ are arbitrary as long as they are perpendicular to $\boldsymbol{n}^{(1)}$, the stability of the stationary solutions (Q_2, Q_3) with the constraint $Q_2^2 + Q_3^2 = 1$ of Eqs. (A.2) and (A.3) should be neutral.

As a result, the analytical form of the stability condition of $\omega = 0$ is calculated from Eq. (39) as follows. For the stationary solutions $Q_1 = 1$ and $Q_2 = Q_3 = 0$, the stability condition of $\omega = 0$ is given from Eq. (39) by $\zeta < \zeta_{st}^-$ with ζ_{st}^- given by Eq. (41). In contrast, for the solutions $Q_1 = 0$ with $Q_2^2 + Q_3^2 = 1$, the stability condition of $\omega = 0$ is given from Eq. (39) by $\zeta < \zeta_{st}^+$ where ζ_{st}^+ is obtained as Eq. (43).

Next, we consider the stability condition of $\omega = 0$ for the circular state. For the circular motion on a plane described by Eqs. (35)–(37), Eq. (40) is represented as

$$\frac{dQ_1}{dt} = [-\mathcal{C}_+(1 - Q_1^2 - Q_2^2) - \mathcal{C}_-(1 - Q_1^2 + Q_2^2)]Q_1 + \frac{\kappa}{2\mathcal{P}}(1 - \mathcal{P}^2)^{1/2} Q_2 \tag{A.4}$$

$$\frac{dQ_2}{dt} = [-\mathcal{C}_+(1 - Q_1^2 - Q_2^2) + \mathcal{C}_-(1 + Q_1^2 - Q_2^2)]Q_2 - \frac{\kappa}{2\mathcal{P}}(1 - \mathcal{P}^2)^{1/2} Q_1 \tag{A.5}$$

$$\frac{dQ_3}{dt} = [\mathcal{C}_+(1 - Q_3^2) + \mathcal{C}_-(Q_1^2 - Q_2^2)]Q_3 \tag{A.6}$$

where $\mathcal{C}_+$ and $\mathcal{C}_-$ are defined as Eqs. (47) and (48), respectively. Here, we have used the condition

$$Q_1^2 + Q_2^2 + Q_3^2 = 1. \tag{A.7}$$

From Eq. (A.7), only two of the Q_m are independent variables and the other is determined from Eq. (A.7). Here, Eqs. (A.4) and (A.5) are independent of Q_3. Therefore, we take Q_1 and Q_2 as independent variables. By defining

$$Q_\pm = Q_1^2 \pm Q_2^2 \tag{A.8}$$

Eqs. (A.4) and (A.5) can be written as

$$\frac{dQ_+}{dt} = -2[\mathcal{C}_+ Q_+ + \mathcal{C}_- Q_-](1 - Q_+) \tag{A.9}$$

$$\frac{dQ_-}{dt} = -2\mathcal{C}_+(1 - Q_+)Q_- - 2\mathcal{C}_-(Q_+ - Q_-^2) + \frac{\kappa}{\mathcal{P}}(1 - \mathcal{P}^2)^{1/2}(Q_+^2 - Q_-^2)^{1/2}. \tag{A.10}$$

Here, we have required that $Q_+^2 - Q_-^2 > 0$ without loss of generality. It is readily seen that the stationary solutions of Eq. (A.9) are given by $Q_+ = 1$ and

$$Q_+ = -\frac{\mathcal{C}_-}{\mathcal{C}_+} Q_-. \tag{A.11}$$

From an ordinary linear stability analysis, the stability condition of the former stationary solution is given by $L_{Q+} < 0$, and otherwise, the latter stationary solution is stable. Here, the bifurcation threshold is defined by

$$L_{Q_+} = 2\mathcal{C}_+ + 2\mathcal{C}_- Q_-. \tag{A.12}$$

First, we consider the stationary solution $Q_+ = 1$. In this case, Eq. (A.10) becomes

$$\frac{dQ_-}{dt} = -2\mathcal{C}_-(1 - Q_-^2) + \frac{\kappa}{\mathcal{P}}(1 - \mathcal{P}^2)^{1/2}(1 - Q_-^2)^{1/2}. \tag{A.13}$$

It is apparent that $Q_- = \pm 1$ is a stationary solution of Eq. (A.13). Here, we may consider only $Q_- = 1$ without loss of generality. Together with $Q_+ = 1$, this leads from their definition in Eq. (A.8) to $Q_1 = 1$ and $Q_2 = 0$, and hence, $Q_3 = 0$ from Eq. (A.7). However, these values of Q_n are not stationary solutions of Eq. (A.4)–(A.6), where the right-hand side of Eq. (A.5) remains finite. This is because we have implicitly required that $Q_1, Q_2 \neq 0$ when we derived Eqs. (A.9) and (A.10) from Eqs. (A.4) and (A.5) by multiplying them by Q_1 and Q_2, respectively. As a result, the pair of stationary solutions $Q_+ = 1$ and $Q_- = 1$ of Eqs. (A.9) and (A.10) may not be considered here.

Now, from $-1 \leq Q_- \leq 1$, we can write $Q_- = \sin\eta$. Then, from Eq. (A.13), we obtain

$$\frac{d\eta}{dt} = -2\mathcal{C}_- \cos\eta + \frac{\kappa}{\mathcal{P}}(1 - \mathcal{P}^2)^{1/2}. \tag{A.14}$$

If $E_\eta > 0$ where E_η is given by Eq. (46), there exists a stationary solution of Eq. (A.14) given by

$$\cos\eta = \frac{1}{2\mathcal{C}_-}\frac{\kappa}{\mathcal{P}}(1 - \mathcal{P}^2)^{1/2}. \tag{A.15}$$

The stability condition of the stationary solution is given from Eq. (A.14) by $\mathcal{C}_- < 0$. Here, we have required that $\sin\eta = Q_- > 0$ without loss of generality. For the stable stationary solution (A.15), Q_- is given by

$$Q_- = (1 - \cos^2\eta)^{1/2} = \frac{E_\eta^{1/2}}{2|\mathcal{C}_-|}. \tag{A.16}$$

Then, the stability condition of the stationary solution $Q_+ = 1$ is written from Eq. (A.12) as Eq. (44). As a result, for the stable stationary solutions $Q_+ = 1$ and Eq. (A.16), the stability condition of $\omega = 0$ is given from Eq. (39) by $\zeta < \zeta_c^-$ where ζ_c^- is given by Eq. (45).

If $E_\eta < 0$, there is no stationary solution of Eq. (A.14) and the value of η increases (decreases) monotonically for $\mathcal{P} > (<)0$, and, hence, the value of Q_- varies from -1 to 1. Then, the stability condition of $Q_+ = 1$ given by Eq. (A.12) should be obtained on the average over $Q_- = \sin\eta$ and it becomes $L^0_{Q_+} < 0$ where

$$L^0_{Q_+} = 2\mathcal{C}_+. \tag{A.17}$$

In the same way, the stability condition of $\omega = 0$ is calculated from Eq. (39) as Eq. (49).

Finally, we consider the stationary solution of Q_+ given by Eq. (A.11). In this case, the right-hand side of Eq. (A.10) becomes linear in Q_-. Therefore, the stationary solution is given by $Q_- = 0$. Then, from Eq. (A.11), $Q_+ = 0$. From the definition Eq. (A.8), these solutions lead to a set of stationary solutions $Q_1 = Q_2 = 0$ and $Q_3 = 1$ of Eqs. (A.4)–(A.6). Since $Q_1 = Q_2 = 0$, Eqs. (A.4)–(A.6) are

not fully equivalent to Eq. (A.9) and (A.10). We need to investigate the stability of $Q_1 = Q_2 = 0$ and $Q_3 = 1$ by analyzing Eqs. (A.4)–(A.6). From Eq. (A.7), Eqs. (A.4) and (A.5) can be written as closed equations of Q_1 and Q_2. Therefore, we can examine the stability of Q_1 and Q_2 separately from that of Q_3. First, we analyze the stability of the stationary solutions $Q_1 = Q_2 = 0$ of Eqs. (A.4) and (A.5) by using the linear stability matrix defined by $L_{ij} = \partial_i (dQ_j/dt)$ where ∂_i represents the partial derivative with respect to Q_i ($i = 1, 2$). The trace and determinant of the linear stability matrix for the stationary solutions $Q_1 = Q_2 = 0$ can be calculated as

$$\mathrm{tr}L = -2\mathcal{C}_+ \tag{A.18}$$

$$\det L = \mathcal{C}_+^2 - \mathcal{C}_-^2 + \left(\frac{\kappa}{2\mathcal{P}}\right)^2 (1 - \mathcal{P}^2) = \mathcal{C}_+^2 - \frac{1}{4} E_\eta. \tag{A.19}$$

The stability of the stationary solutions $Q_1 = Q_2 = 0$ is given by $\mathrm{tr}L < 0$ and $\det L > 0$. As long as this stability condition is satisfied, we find from Eq. (A.6) that $Q_3 = 1$ is stable. As a consequence, the stability condition of $\omega = 0$ for the solutions $Q_+ = Q_- = 0$ is obtained as Eq. (51) from Eq. (39).

References

[1] K. Keren, Z. Pincus, G. M. Allen, E. L. Barnhart, G. Marriott, A. Mogilner, and J. A. Theriot, Nature, **453**, 475 (2008).
[2] L. Bosgraaf and P. J. M. Van Haastert, PLoS ONE, **4**, e5253 (2009).
[3] L. Li, S. F. Norrelykke, and E. C. Cox, PLoS ONE, **3**, e2093 (2008).
[4] Y. T. Maeda, J. Inoue, M. Y. Matsuo, S. Iwaya, and M. Sano, PLoS ONE, **3**, e3734 (2008).
[5] K. Nagai, Y. Sumino, H. Kitahata, and K. Yoshikawa, Phys. Rev. E, **71**, 065301(R) (2005).
[6] H. Kitahata, N. Yoshinaga, K. Nagai, and Y. Sumino, Phys. Rev. E, **84**, 015101(R) (2011).
[7] H. Wada and R. R. Netz, Phys. Rev. E, **80**, 021921, (2009).
[8] T. Ishikawa, J. R. Soc. Interface, **6**, 815 (2009).
[9] S. I. Nishimura, M. Ueda, and M. Sasai, PLoS Comput. Biol., **5**, e1000310 (2009).
[10] S. Günther and K. Kruse, Europhys. Lett., **84**, 68002 (2008).
[11] G. P. Alexander and J. M. Yeomans, Europhys. Lett., **83**, 34006 (2008).
[12] H. Boukellal, O. Campás, J.-F. Joanny, J. Prost, and C. Sykes, Phys. Rev. E, **69**, 061906, (2004).
[13] W. L. Zeile, F. Zhang, R. B. Dickinson, and D. L. Purich, Cell Motil. Cytoskeleton, **60**, 121 (2005).
[14] H. C. Crenshaw, Am. Zool., **36**, 608 (1996).
[15] V. B. Shenoy, D. T. Tambe, A. Prasad, and J. A. Theriot, Proc. Natl. Acad. Sci. USA, **104**, 8229 (2007).
[16] W. R. DiLuzio, L. Turner, M. Mayer, P. Garstecki, D. B. Weibel, H. C. Berg, and M. Whitesides, Nature, **435**, 1271 (2005).
[17] K. Drescher, J. Dunkel, L. H. Cisneros, S. Ganguly, and R. E. Goldstein, Proc. Natl. Acad. Sci. USA, **108**, 10940 (2011).
[18] F. Takabatake, N. Magome, M. Ichikawa, and K. Yoshikawa, J. Chem. Phys., **134**, 114704 (2011).
[19] T. Ohta and T. Ohkuma, Phys. Rev. Lett., **102**, 154101, (2009).
[20] T. Ohta, T. Ohkuma, and K. Shitara, Phys. Rev. E, **80**, 056203, (2009).
[21] K. Shitara, T. Hiraiwa, and T. Ohta, Phys. Rev. E, **83**, 066208, (2011).
[22] T. Hiraiwa, M. Y. Matsuo, T. Ohkuma, T. Ohta, and M. Sano, Europhys. Lett., **91**, 20001 (2010).
[23] T. Hiraiwa, K. Shitara, and T. Ohta, Soft Matter, **7**, 3083 (2011).
[24] R. Wittkowski and H. Löwen, Phys. Rev. E, **85**, 021406, (2012).
[25] M. Tarama and T. Ohta, J. Phys.: Condens. Matter, **24**, 464129 (2012).
[26] M. Tarama and T. Ohta, Eur. Phys. J. B, **83**, 391 (2011).
[27] E. Ott, *Chaos in Dynamical Systems* (Cambridge University Press, Cambridge, UK, 2002).
[28] N. Korabel and E. Barkai, Phys. Rev. Lett., **102**, 050601, (2009).
[29] T. Akimoto and Y. Aizawa, Chaos, **20**, 033110 (2010).
[30] G. M. Zaslavsky, Phys. Rep., **371**, 461 (2002).